# ~~Deposition Velocity in the Presence/Absence of E6-Glass Fibre on Extrusion-based 3D Printed M~~Effects of deposition velocity in the presence/absence of E6-glass fibre on extrusion-based 3D printed mortar

Pshtiwan Shakor[a,*]

pshtiwan.shakor@uts.edu.au

Shami Nejadi[a]

Sheila Sutjipto[b,*]

sheila.sutjipto@uts.edu.au

Gavin Paul[b]

Nadarajah Gowripalan[a]

[a]School of Civil and Environmental Engineering, Ultimo, NSW, 2007, Australia

[b]School of Mechanical and Mechatronic Engineering, Ultimo, NSW, 2007, Australia

*Corresponding authors.

**Abstract**

Additive Manufacturing (AM) technologies are widely used in various fields of industry and research. Continual research has enabled AM technologies to be considered as a feasible substitute for certain applications in the construction industry, particularly given the advances in the use of glass fibre reinforced mortar. An investigation of the resulting mechanical properties of various mortar mixes extruded using a robotic arm is presented. The nozzle paths were projected via 'spline' interpolation to obtain the desired trajectory and deposition velocity in the reference frame of the manipulator. Along each path, various mortar mixes, with and without chopped glass fibre, were deposited at different velocities. Tests were conducted to determine their mechanical performance when incorporated in printed structures with different layers (1, 2, 4 and 6 layers). The results are compared with those of conventional cast-in-place mortar. In this study, the mixes consist of ordinary Portland cement, fine sand, chopped glass fibres (6 mm) and chemical admixtures, which are used to print prismatic- and cubic-shaped specimens. Mechanical strength tests were performed on the printed specimens to evaluate the behaviour of the materials in the presence and absence of glass fibre. Robot end-effector velocity tests were performed to examine the printability and extrudability of the mortar mixes. Finally, horizontal and vertical line printing tests were used to determine the workability, buildability and uniformity of the mortar mix and to monitor the fibre flow directions in the printed specimens. The results show that printed specimens with glass fibre have enhanced compressive strength compared with specimens without glass fibre.

**Keywords:** Extrusion printing; End-effector speed; Printed multi-layers; Mechanical properties; Glass fibre reinforced mortar

# 1 Introduction

The construction industry continually faces financial challenges, placing pressure on productivity, profitability, and the integration of new technologies [1–3]. However, three-dimensional printing (3DP) is emerging in the construction industry, challenging traditional construction methods. In its inception, the emphasis of 3DP was to quickly create scaled models for visualisation throughout product development. Advancements in technology have improved the accuracy and quality of such models [4], and experimentation with novel materials and the scale of printed specimens continue to be active areas of research [5,6].[cite57]

To address the construction of large-scale structures, various approaches to concrete 3DP have been reported in the literature, notably the concept of 2.5D printing realised by means of overhead cranes [6,7][cite 58] and, in more recent years, the utilization of industrial manipulators [8]. The transition to industrial manipulators is seen to address certain limitations imposed by the aforementioned methods [9], in particular, the reduced degrees of freedom limiting the systems' ability to manoeuvre the printhead in various orientations [10]. Furthermore, manipulators possess larger possible build volumes and address the issue of portability when compared to their crane and gantry style counterparts. Thus, research continues to explore the incorporation of industrial robotic arms in such systems to investigate and improve the ability to construct complex structures [8,11,12] and to determine the viability in the

construction industry [13,14].

The capability of a robot to print complex 3D structures is highly dependent upon the control methodology used for the robotic arm. A popular choice for the online control of robotic arms is differential kinematics, however, an inherent problem associated with this technique are kinematic singularities. Singularities result in undesired motions such as oscillations at the end-effector causing uneven or discontinuous surfaces when printing mortar and concrete members, or potentially erratic unpredictable motions of the robot arm. These consequences can be detrimental to both the printed structure and the robot's surrounding environment. This behaviour is a well-understood problem of robotic arms and, consequently, methods have been developed to ensure the safe and predictable operation of robotic arms near such configurations. Studies have documented the influence of Damped Least Squares (DLS) on the robotic arm's joint velocities to mitigate the effect of singularities when obtaining inverse kinematic solutions [15], during physical human-robot interaction [16] and in concrete 3DP [17].

The consideration of safe robot movements is only one facet of robot safety. Although safe robot movements were initially concerned with the safety of the robot and its environment, segregating robots from humans, the shift towards collaborative workspaces has focused on the safety of humans working within the robot's operational space [18]. Industry standards, such as [19,20], have since defined collaborative workspaces, suggesting various techniques to be implemented for collaborative operations. Early research considered reduced end-effector speeds [21] based upon human reaction times; however, the robot's potential capabilities are limited regardless of the presence of humans. Consequently, improved sensing capabilities have enabled this strategy to be combined with human detection algorithms. In this way, a robot could be stopped or could continue to function with a different mode of operation [23]. Some possible modes of operation include limited end-effector, joint speeds/torques based upon the presence of humans in a predefined zone surrounding the robot, or scaled based upon the separation distance between the human and robot. Without the implementation of such safety strategies, industrial robots will continue to exist behind physical barriers.

The incorporation of digital fabrication into the construction industry introduces concerns surrounding the integrity and digital security of the printed specimen. As various data formats are susceptible to malicious modifications, processes must be implemented to ensure that data has not been tampered with before commencing fabrication. Such modifications could foreseeably jeopardize the structural integrity of the specimen or could endanger operators working within the robot workspace through unpredictable movements [22,23].

Although systems encompassing robotic arms are becoming prevalent, further investigation is still required to discern the effects of robot end-effector travel speed, trajectory shape, end-effector orientation and feed pump properties on printed structures [24,5,25,26]. In particular, Xu, Ding, Cai, Zhang, Luo and Qin [27], explored the effect of the nozzle travel speed. In their study, a stable travel speed for the end-effector nozzle was assumed, whilst the speed of the material delivery deposition and the size of the nozzle varied. With a similar hardware setup, [28] explored the effect of cement mortar filament output speeds. It was shown that both the nozzle travel speed and material flow rate affect the setting time of the printed parts. Again, a limitation of [28] is in the utilization of a rigid gantry frame. However, printing using a 6-DOF robotic arm faces further challenges pertaining to the systems' ability to track a trajectory and the motion of the end-effector.

The delivery system is an integral component of the hardware setup that must be synchronised and tuned with the motion of the robot. It affects the outcome of the printed structure by influencing the shapeability and slump of the concrete or mortar [1,29,30]. Pumps are the most common delivery system incorporated in concrete printing applications. There exists a range of pump types, each possessing physically varying structures and functions that affect the delivery of material between the source and the extruder. Previous works have explored the implementation of various pumps for the purpose of printing mortar or concrete structures including, but not limited to, the progressive cavity pump [31] see Fig. 1, peristaltic pump [8], pneumatic pump [13], and piston pump [32]. Each pump possesses inherent limitations such as pressure, flow rate, and loss of energy through heat. In addition, the transfer of heat from the pump to the slurry affects the consistency of the mortar mix. This unintentional heat transfer can affect the mechanical behaviour of the printed element and the shapeability or microstructure of the printed mortar. However, pneumatic, centrifugal and peristaltic pumps produce fewer cavities and air voids in the printed specimens than the progressive cavity pump. This is due to their ability to limit air entrainment, due to the working principle of the turbine, and reduced abrasion [33].

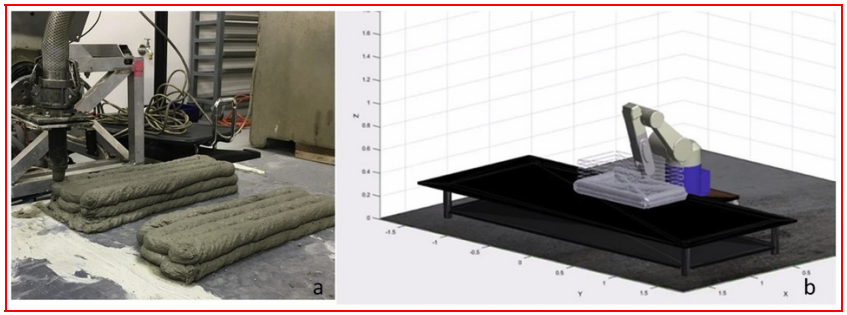

**Fig. 1** (a) Real-world concrete 3D printing setup with a 6-DOF robot arm. (b) Simulated MATLAB model of the robot arm showing the partially-complete and planned concrete print path.

alt-text: Fig. 1

A major factor influencing the choice of pump is the type of fibre-reinforced mix that needs to be transported. Earlier studies used polypropylene (used a polypropylene) (PP) fibre-reinforced mix to demonstrate the viability of the 3D printing of fibre-reinforced mortar mixes. However, with PP fibre-reinforced mixes, it was observed that clogging occurred whilst pumping, meaning the combination of this delivery system and this material required further refinement. For PP types of fibre, they can be delivered via a caulking gun and (Previous work has shown that polypropylene types of fibre can be delivered via a caulking gun and) a Ø 50 mm [31] hose; however, when the nozzle and hose are reduced to Ø20 mm, the PP fibre is unable to travel through the narrow hose at the end of the stator. An additional limitation, which is otherwise not considered in other studies, is that the dimension of PP fibre is 6 mm in length and 100 µm in diameter.

To reflect real-world construction applications, E-glass fibre has been incorporated for non-prestressed applications [34], where it was combined with the mortar mix to minimise instances of clogging and damage to the fibres. It is noted that an alternative material that can be incorporated in 3D printed mortar is straight steel fibre, which has been demonstrated to increase the flexural strength of printed prisms [35]. Another study by [36], explored the effect of glass fibre in geopolymer concrete using various strand length (3 mm, 6 mm, 8 mm). It was observed that an addition of 1 % glass fibre, for each respective strand length, improves the mechanical behaviour of the specimens. Similar to paper [28,36] has also printed their small scale of specimens using 4-axis gantry. In addition to exploring the effect of fibre strand length on the mechanical behaviour of the specimens, the effect of alternative fibres such as aramid, basalt and carbon, should be examined.

This paper demonstrates the effect of the deposition nozzle's velocity on the width of the printed mortar and properties of the deposited slurry, whilst maintaining a constant pump setting. The resulting mechanical behaviour of the printed structures in the presence and absence of chopped glass fibres is also presented.

# 2 Materials

The materials used in this paper comprised (comprised of) ordinary Portland cement complying with Australian Standard (AS 3972) general-purpose cement, fine sand (150~425 µm) (called Sydney sand) and chemical admixtures such as superplasticizer (Sikaplast), a retarder (Retarder N) and accelerator (Sigunit L80AF). Fig. 2 displays the particle size distributions of fine sand and ordinary Portland cement. The use of chemical admixtures such as superplasticizer, retarder and accelerator dictate the open and setting time of the mortar [37,38].

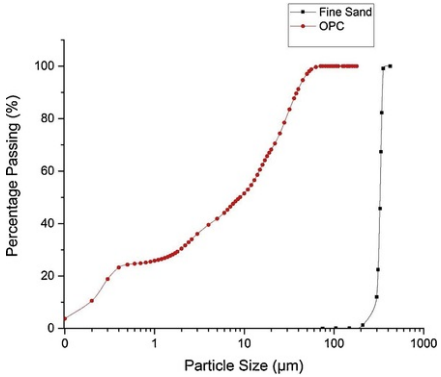


**Fig. 2** The percentage passing of the ordinary Portland cement and fine sand versus particle size [31].

alt-text: Fig. 2

This study tests the incorporation of various amounts of glass fibre, which is known as E6-glass fibre (high-performance E6 enhanced glass fibre). Table 1 summarises the physical properties of this glass fibre [39] with fibre dosage used being 1 % by weight of cementitious powder. In addition to the environmental benefits of E6-glass fibre, this fibre improves temperature resistance, resistance to acid corrosion, elastic modulus, and mechanical properties such as compressive and shear strength [40]. These properties have led to the selection of E6-glass fibre for printing applications. As mentioned earlier, it is known that PP fibre can be troublesome (difficult to use) in the printing process due to its tendency to clog within the delivery system. Thus, considerations have been made about suitable hardware to deliver the selected material.

**Table 1** Physical properties of chopped E6-glass fibres.

alt-text: Table 1

| Fibre type | Length (mm) | Diameter (µm) | Filament diameter (mm) | Specific gravity (g/cm³) | Tensile strength (MPa) | Tensile modulus (GPa) | Expansion coefficient ($10^{-6}$ $K^{-1}$) |
|---|---|---|---|---|---|---|---|
| E6-Glass fibre (Trojan) | 6 ± 1 | 100 | 13 ± 1 | 2.62-2.63 | 2500-2700 | 81 | 6 |

# 3 Methods

## 3.1 Physical and ~~Mechanical C~~mechanical characterisation

The physical properties of the materials define the mechanical characterisation and strength of the specimen. Therefore, the proportion of materials present in the concrete mixture is crucial for improved shapeability and buildability of the printed structures.

Several trials were previously conducted using varying material ratios to ascertain a combination capable of being printed from a nozzle and transported through a progressive cavity pump and delivery hose [31]. The trials considered the slump and smooth flow of the cement mortar and aimed to minimise the air entrainment and material blockage. Table 2 presents the optimum mortar slurry that is capable of being transported through the pump and delivery system.

**Table 2** Optimal mortar mix design for a progressive cavity pump system.

alt-text: Table 2

| Fine Sand (g) | Cement (g) | Sand/cement ratio | Retarder (ml) | Accelerator (ml) | Superplasticizer (ml) | Water (ml) | w/c ratio | E6-Glass Fibre |
|---|---|---|---|---|---|---|---|---|
| 6075 | 5062.5 | 1.2 | 27 | 33.75 | 25.31 | 1890 | 0.31 | 0% |
| 6075 | 5062.5 | 1.2 | 27 | 33.75 | 30 | 2000 | 0.33 | 1% (111.375 g) |

Table 3 summarises the types of specimens and the number of specimens fabricated. The nozzle diameter selected was Ø 20 mm, based on previous studies by the author [17].

**Table 3** Dimensions of the specimens for printed specimens and conventional moulds.

alt-text: Table 3

| Specimen description | Number of layers | Number of specimens | CAD dimension of specimens (mm)[a] | Delivery method |
|---|---|---|---|---|
| Printed cubes with/without fibre reinforced mortar | 1 | 6 | 20 × 20 × 20 | Progressive cavity pump (Ø20 mm) |
| | 2 | 6 | 40 × 40 × 40 | |
| | 4 | 6 | 80 × 80 × 80 | |
| | 6 | 6 | 120 × 120 × 120 | |
| Printed prisms with/without fibre reinforced mortar | 1 | 6 | 120 × 20 × 20 | Progressive cavity pump (Ø20 mm) |
| | 2 | 6 | 160 × 40 × 40 | |
| | 4 | 6 | 220 × 80 × 80 | |
| | 6 | 6 | 260 × 120 × 120 | |
| Casted cubes | – | 24 | 50 × 50 × 50 | Conventional method |
| Casted prisms | – | 24 | 160 × 40 × 40 | |

[a] The size of specimens are approximations, and dimensions vary from specimen to specimen.

Fig. 3 shows two specimens with 6 and 4 printed layers, and with/without E6-glass fibre reinforcement, respectively. The figures show that when glass fibre is present during printing fabrication, the shape of the printed lines and layers can change undesirably.

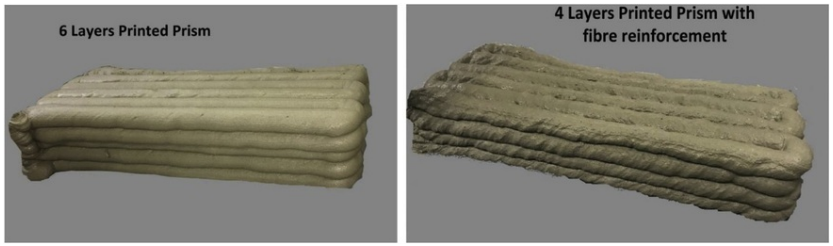


**Fig. 3** Printed mortar prisms and cubes realised via a robotic arm without (left) [31] and with (right) glass fibre reinforcements.

alt-text: Fig. 3

To assess the mechanical properties of different mortar batches before printing specimens, a uniaxial compressive strength test of cube specimens was conducted. Cubes of 50 × 50 × 50 mm were prepared according to Australian standards [41]. The loading rate applied was 0.83 kN/s. The devices used were Shimadzu (UH-500 kN XR 500 kN, Japan) and (UH-2000kN, Japan) for the uniaxial compressive strength test.

To evaluate the flexural strength of the specimens, a three-point bending test was applied to the mortar mixes [42]. The prisms were cast as conventional control specimens with dimensions of 160 × 40 × 40 mm. The machine used to conduct the flexural strength test was the Shimadzu (AGS-X 50 kN, Japan). The loading rate applied was 0.43 kN/min.

The mortar specimens for the three-point bending test were printed using the robot. Table (3) demonstrates that the printed specimens possess the same dimensions as the prism (120 × 20 × 20 mm for one layer; 160 × 40 × 40 mm for two layers; 220 × 80 × 80 mm for four layers; and 260 × 120 × 120 mm for six layers). All printing processes utilised a 20 mm circular nozzle, where the overall width, thickness and length of the structures varied (Table 3). Six specimens for each of the “number of layers” tests were printed in the presence and absence of glass fibres. The fabrication of the specimens used a constant end-effector velocity of 46.56 mm/s. A time gap of 10 min~~utes~~ between each vertically printed layer was selected based on previous studies [26,39–41]. This time gap can be determined according to the mortar mix proportions, water content, humidity and time of mixing.

## 3.2 Robotic ~~System H~~system hardware

To manufacture the concrete specimens for experimentation, a custom-made setup was developed, as shown in Fig. 4 Top-down view of the hardware setup for concrete 3D printing. Fig. 4. The robotic arm used for the experimentation was the Denso-VM6083-W, controlled via the proprietary controller. The arm was mounted on a custom frame with a linear rail; however, the base was fixed for these experiments. A bespoke end-effector tool was designed to extrude the mortar mixtures when using the progressive cavity pump unit, where the extruded material was deposited onto laminated particleboard. The delivery system was mounted on a trolley jack allowing the pump to be elevated to varying heights to encourage slurry discharge and to improve mortar performance. A steel hopper was used to hold material before it entered the pump through the pump inlet, the pump then delivered the mixture to the end-effector via the pump outlet and tubing interface.

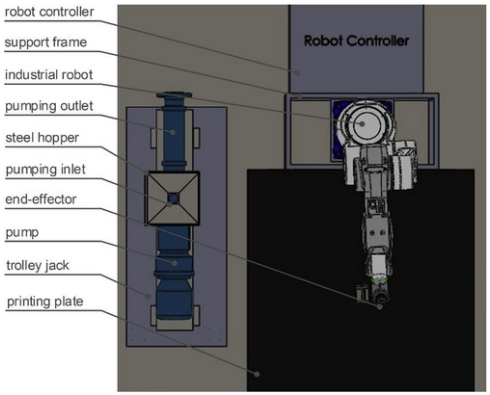

**Fig. 4** Top-down view of the hardware setup for concrete 3D printing.

alt-text: Fig. 4

## 3.3 Robot ~~Deposition T~~deposition toolpath

The two structures printed by the system are referred to as horizontal and vertical tests. Fig. 5 illustrates the cross-section of the specimens. The toolpath required to deposit the material so it achieves the illustrated cross-section can be projected via spline interpolation, where the desired trajectory is defined with respect to the robot base frame, $b$. Thus, the pose at any location in the toolpath can be expressed by the following homogeneous transformation matrix,

$$ {}^{b}T_{e} = \begin{bmatrix} {}^{b}R_{e} & {}^{b}p_{e} \\ 0_{1\times3} & 1 \end{bmatrix} \varepsilon\ \mathrm{SE}(3) \quad (1) $$

Where, ${}^{b}T_{e}$ is the homogeneous transformation matrix representing the pose of the end-effector relative to the robot base frame, ${}^{b}R_{e}$ is the rotation matrix of the end-effector relative to the robot base frame, and ${}^{b}p_{e}$ defines the position of the end-effector relative to the robot base frame.

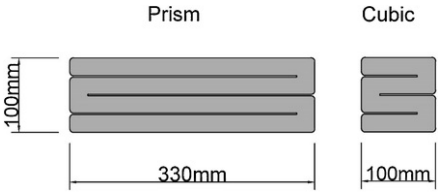


**Fig. 5** Horizontal printed path cross-section “four lines printed specimen”.

alt-text: Fig. 5

The horizontal and vertical tests differed with the number of layers in the structure, namely, one layer and greater than one layer, respectively. When represented as a homogeneous transformation matrix, the toolpath can be translated above the initial layer, constructing the toolpath for sequential layers.

The end-effector pose of the robot can be defined as a vector with $m$ entries representing the dimension of the task space, $x \varepsilon \mathbb{R}^{m}$. Similarly, the joint angles of the robot can be expressed as a $n$-dimensional vector, $q \varepsilon \mathbb{R}^{n}$, where the two vectors are related as

(Equation (2) – there is no full stop after the equation.)

$$ x = f(q) \quad (2) $$

~~x = f(q) .~~ x = f(q)

The time derivative of (2) results in (3) where the end-effector velocities, $\dot{x}$, and joint velocities, $\dot{q}$, are mapped by the Jacobian,

$$ \dot{x} = \frac{\partial f(q)}{\partial q}\dot{q} \quad (3) $$

$$ \dot{x} = J(q)\dot{q} \quad (4) $$

where, $J(q)$ is the Jacobian matrix of the manipulator, given a joint configuration, $q$.

Since the end-effector is required to move at a constant speed throughout the prescribed trajectory, solving for $\dot{q}$,results (needs a space between comma and "results") in a set of joint velocities that satisfy the aforementioned requirements and the poses defined in the toolpath.

## 3.4 Robot ~~Build Volume M~~build volume maximisation

In this mortar printing task, an industrial robot is used since it possesses a larger build volume relative to its physical size, and tool path flexibility when compared to a crane or gantry style setup. However, there are some challenges when printing near the extremities of the build volume. As the desired motion of the robot is defined in the task space of the robot, the end-effector motion may approach configurations that correspond to a kinematic singularity. This occurs when the Jacobian matrix loses rank, where $\mathrm{rank}\,(J(q)) < m$. A poorly conditioned Jacobian matrix can result in undesired robot motions detrimental to the structure printed, as well as unsafe motions in the

workspace. To determine whether the configuration of the arm is near singular, the Measure of Manipulability can be defined by a scalar value as proposed by Yoshikawa [43],

$$w = \sqrt{J(\mathrm{q}) * J^T(\mathrm{q})} \quad w = \sqrt{detJ(\mathrm{q}) * J^T(\mathrm{q})} \tag{5}$$

(Equation(5)- missing "det", check attachment)

As the system approaches near singular configurations, the scalar value, $w$, representing the measure of manipulability approaches 0.

Since this is a well-explored issue in robotics, there are various methods that can be used to address the resulting undesired behaviour. One such solution is the Damped Least Squares method [15], which compromises between end-effector error and the condition of the Jacobian matrix near singularities. The exactness of the solution and feasibility are evaluated simultaneously by minimising the norm of both terms,

$$\min \left\{ \left\| \dot{\mathrm{x}} - J(\mathrm{q})\dot{q} \right\|^2 + \lambda^2 \left\| \dot{q} \right\|^2 \right\} \tag{6}$$

Solving (6) corresponds to,

$$\dot{\mathrm{x}} = J^*(\mathrm{q})\dot{\mathrm{q}}\#$$
$$\dot{\mathrm{q}} = J^*(\mathrm{q})^{-1}\dot{\mathrm{x}}\#$$

(Equation (7) – first equation is confusing and redundant (i.e. incorrect and should be removed), Equation (7) should just be the following line: check the attachment.) **(7)**

$$J^*(q) = J(\mathrm{q})^T \left( J(\mathrm{q}) J(\mathrm{q})^T + \lambda^2 I \right)^{-1} \tag{8}$$

The damping factor sets a weighting term to the velocity component. Smaller values of $\lambda$ give more exact solutions but are less robust in instances where the robot is in singular or near singular configurations, such as when depositing mortar at the extremities of the robot's workspace. However, greater values of $\lambda$ have poorer tracking accuracy regardless of whether a feasible and accurate solution is possible. Thus, when applied correctly the weighted pseudo-inverse of the Jacobian is robust to singularities, and longer continuous deposition paths are possible while the build volume is enlarged.

## 3.5 Printing Aaccuracy

The behaviour of the robot with a constant damping factor, $\lambda$, does not necessarily ensure stability or exactness when within the neighbourhood of singular points or outside the boundaries, respectively. This can lead to costly inaccuracies and structural instability when depositing multiple layers of material. Thus, in instances where the configuration is singular, the damping factor $\lambda$ should represent a larger scalar value. The adjustment of the damping factor can be defined as a function of the Measure of Manipulability [43],

$$\lambda = \begin{cases} \lambda_0 \left( 1 - \frac{w}{w_0} \right)^2, & w < w_0 \\ 0, & w \geq 0 \end{cases} \tag{9}$$

(Equation (9) – second line changed from "0" to " $w \geq w_0$". check the attachment)

Where, $\lambda_0$ is a scale factor acting in the region of singular points, and $w_0$ is a threshold that outlines the boundary of the singular region defined by the Measure of Manipulability. Defining $\lambda_0$ and $w_0$ is critical for this method as it affects the behaviour of the robot, as well as its performance when tracking a trajectory.

The executed commands of the robot are defined as a series of joint velocities calculated using (Eq. (7)) (7) . During a pre-planned print, the desired deposition location for the nozzle and the joint configuration of the robot is known at any point throughout the trajectory. Forward kinematics can then be used to obtain the position error of the end-effector. Thus, given the current and following the desired waypoint, as well as the control frequency of the system, a corrective translational end-effector velocity can be determined. The orientation error is calculated using an approximation of the derivative of the rotation matrix, R (see ~~equation~~Eq. (1)), where the corrective orientation end-effector velocity is extracted via the skew-symmetric matrix. This ensures that the induced printing errors, from mitigating undesired motions at kinematic singularities, are addressed by incorporating feedback control.

## 3.6 Safety Cconsiderations

The velocity at which the 3DP nozzle affixed to the end-effector travels is determined by several factors. Generally, the required velocity can be determined by the desired thickness of the layer, reflected in the choice of the mortar mix proportions and the pump flow rate. Another aspect influencing the end-effector speed for the experiments is safety. Segregating robots from humans is often undesirable due to the complementary capabilities of humans.

Human-robot interaction is an important opportunity, which holds great potential for the future of AM in the construction industry. However, the presence of humans in the robot workspace requires consideration of the motion of the robot and the response time of the human reacting to unforeseen occurrences. Safe end-effector speeds have been investigated [21] based upon these human reaction times. Hence, in this present research, a robot end-effector speed limit was imposed. A maximum speed of 34.99 mm/s was used when printing the prismatic and cubic specimens, which adheres to the safely reduced speeds that were initially outlined by [21].

## 3.7 Progressive ~~Cavity P~~cavity pump

The progressive cavity pump, consists of a small sequence of fixed-shape discrete cavities that are filled and emptied as the rotor is turned. The rotation rate (bidirectional) and low levels of shearing applied to the pumped liquid causes a volumetric flow rate to be pumped proportionally [44]. Throughout all 3DP tests presented in this paper, the progressive cavity pump was set to the "low" running speed, which for the pump is the lowest flow rate defined as #1(~2 $m^3$/h) out of #10(~200 $m^3$/h) [45].

For this study, mortar slurry was selected due to its ability to flow through the progressive pump. The coarse aggregate was ignored for this experiment to minimise damage to the rubber cover in the stator of the pump. In this investigation, glass fibre was selected as the reinforcement for the mortar, as described in Section 2. This pump was selected due to its appropriate flow rate range and outlet size.

The flow rate of the pump and slurry discharge of the mortar are assumed to increase linearly, based upon a study by El-Haroun [46], which observed that the wind pump linearly discharges with the flow rate of the pump.

Previous studies have explored the behaviour of the slurry while printing [47]. It was proposed that slurry-like materials possess thixotropic rheological behaviour, explaining the ability of the mixture to flow through a delivery system. Thixotropy is described as a material's reduced viscosity when stress is applied to the material (e.g. mixing, stirring, shaking). Reduced viscosity can occur during the pumping process causing the material to flow smoothly and to be extruded through the delivery system.

# 4 Results and ~~D~~discussions

## 4.1 Physical and ~~Mechanical C~~mechanical characterisation

When fibre is incorporated properly as a reinforcement aid, it can improve the behaviour of the resulting material. Compton and Lewis [48] developed a lightweight cellular composite material by adding carbon fibre with a diameter 10 μm, and a length of 220 μm. They observed that a high ratio of carbon fibre alignment was horizontal to the printing flow process, resulting in a role that can be characterised as reinforcement. In [39], glass fibre filament with a diameter of 13 μm and total chop length of 6000 μm was incorporated into printed parts. They showed and were supported by the results from Hambach and Volkmer [49], that the fibre orientation and alignment were parallel to the print flow directions, and the alignment of the fibre, as it passed through the nozzle, was congruent with the printing flow. Experiments have been conducted to determine whether this trend is observed in larger-scale specimens when using a long hose and large pump, and results show how the (and the results have shown how the) orientation (or absence) of glass fibres can affect the compressive strength.

In this paper, a laser scanning microscope has been used to quantify the directionality of the glass fibre in 3D printed cubic and prismatic specimens. Using the scanning microscope, it was observed that approximately 80 % of the fibre orientations in the specimen shown in Fig. 6 aligned with the nozzle's direction of travel. This observation also supports the findings in [48] where carbon fibres were shown to be aligned with the raster direction of the 3DP composite polymer materials. A region of the specimen was selected to ascertain the fibre orientation (refer to Fig. 7. Since this scan requires high magnification, it was essential that each specimen possessed a smooth surface. To achieve this, the printed specimens were cut by a concrete cutting machine.

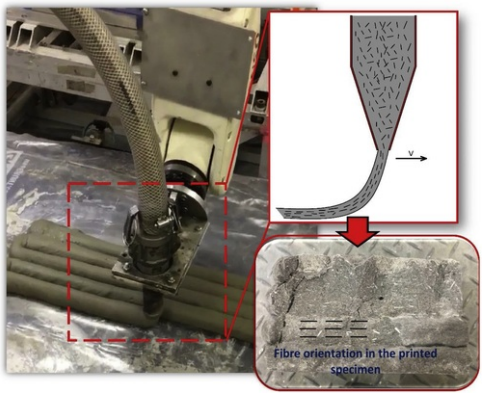

**Fig. 6** Fibre orientation in the printed specimens after crashed under the uniaxial compressive strength test.

alt-text: Fig. 6

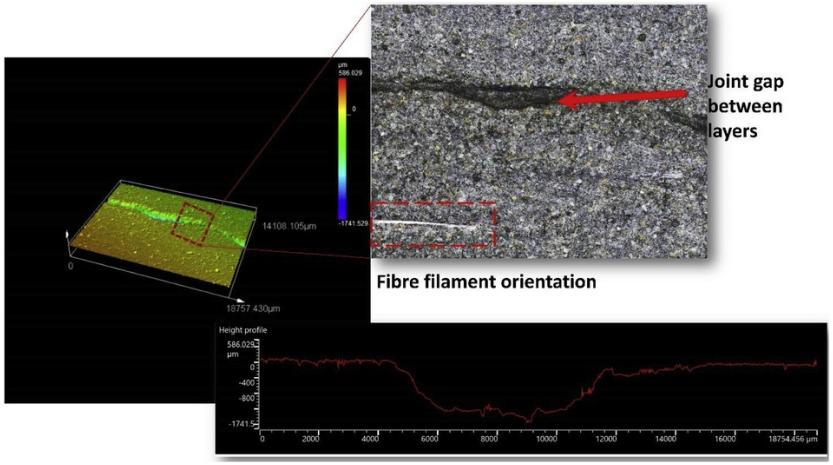


**Fig. 7** Fibre orientation embedded in horizontal layers, and the joint gap between layers; surface roughness illustrated by the 3D laser scanner.

alt-text: Fig. 7

Figs. 6 and 7 illustrate the fibre dispersion after printing, and the dimensions of the fibre in its original condition in the mortar mixture, respectively. This supports the observations made during the printing process and after the uniaxial loading test. It is demonstrated that the fibre filaments are not damaged during any process of experimentation, most notably during the mixing process, and whilst the material is being transferred through the pump and hose. In Fig. 7, a gap (6000 µm wide and 1700 µm deep) can be observed between the top and bottom layers. These gaps contribute significantly to the reduced mechanical strength of the specimens.

A section of the printed mortar was cut by the concrete cutting machine to further inspect the existing gaps between layers and to find open pores in the specimen. ImageJ (image processing software) was used to ascertain the number of fibres embedded in the printed specimens. Through ImageJ, the image can be adjusted by selecting a colour threshold, then the average diameter and area of the specimen can be obtained by measuring and analysing the features. Fig. 8 shows that voids possessing an average diameter of $350.24 \pm 101$ µm are present on the surface of the printed specimens. These voids could be a consequence of chemical additives used, such as the superplasticizer, or the pumping action caused during mortar delivery.

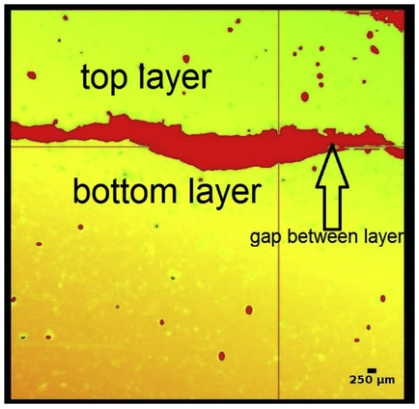


**Fig. 8** Voids and gaps between layers are distinguished from the printed surface using the colour red-threshold (For interpretation of the references to colour in this figure legend, the reader is referred to the web version of this article.).

alt-text: Fig. 8

Fig. 9 depicts a 15.5 ×× 11.1 mm area of the printed specimen. This specimen was used to determine the orientation of the fibre in the printed specimen. By selecting 6 fibre filaments from Fig. (9), it was determined that the fibre parallel to the printed line possesses an orientation angle of -10.05°±7.65, see Table 4.

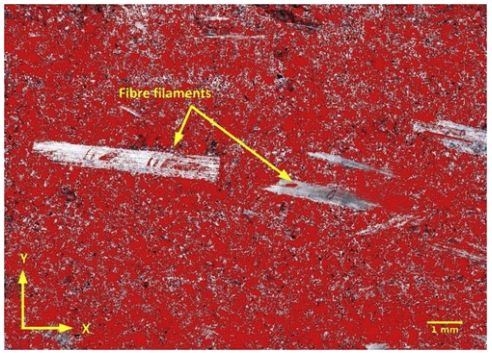


**Fig. 9** Image of the surface of the printed specimen after colour thresholding to indicate the fibre filaments on the surface of the printed specimen.

alt-text: Fig. 9

**Table 4** Fibre orientation and pores in the printed specimens.

alt-text: Table 4

| Area of specimens (mm) | Fibre length (mm) | Orientation angle of fibre (°) | Pores on the specimen (µm) |
|---|---|---|---|
| 15.5 × 11.1 | 6 | -−10.05 ± 7.65 | 350.24 ± 101 |

To verify, the compressive stress is calculated according to the equationEq. (10):

$$\sigma = \frac{f}{lb} \tag{10}$$

where $l$ is the length, $b$ is the width of the specimen, and $f$ is the maximum applied force on the specimen.The flexural stress can be calculated using the equationEq. (11)

$$\sigma = \frac{3fl}{2bd^2} \tag{11}$$

where $d$ represents the thickness of the specimens. All specimens were cured in a tap water bath for 28 days before being tested for compressive and flexural strength properties.

A comparison of the cubic mortar specimens with reinforcement is shown in Fig. 10, where the compressive strength values were calculated according to equationEq. (10). Fig. (10) highlights the varying degrees of performance-based upon the number of layers in the structure. The standard deviation between the 6 specimens differs vastly due to the existence of fibre in the printed structures. The compressive strength of the specimens gradually decreased as the number of layers in the structure is increased. This behaviour was expected due to the increasing number of voids with each layer, and the larger dimension of the specimens.

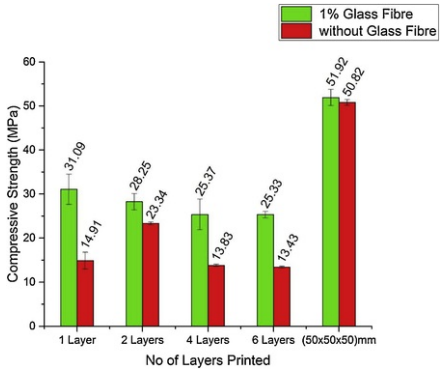


**Fig. 10** Compressive strength results (MPa) of cubic specimens containing 1% glass fibre cured in a tap water bath for 28 days.

alt-text: Fig. 10

The total horizontal print line width for 4 layers was 100 mm, whilst the width of the deposited slurry for one line was approximately 24 mm. The increased number of layers, both vertically and horizontally, contribute to the loss of material strength. Another contributing factor is slumping in the layer thickness caused by the process of printing successive layers of concrete. This phenomenon is also observed during the process of fabricating 3DP polymers [50].

The compressive strength of the printed specimens containing glass fibre reinforcement is outlined in Table 5. The measured compressive strength for the $50 \times 50 \times 50$ mm specimen is $51.92 \pm 1.85$ MPa, a relatively high result compared to other printed specimens. The compressive strength of the cubic mould is approximately 45.59% higher than the 2-layer printed cubes with 1% glass fibre.

**Table 5** Results of the compressive strength for the printed specimens and conventional specimens.

alt-text: Table 5

| Specimen description | Actual dimensional area under uniaxial loading machine (mm) | Compressive strength with 1% glass fibre (MPa) | Compressive strength without glass fibre (MPa) |
|---|---|---|---|
| 1 layer | 19.18 ± 0.34, 18.56 ± 0.61 | 31.09 ± 3.43 | 14.91 ± 1.91 |
| 2 layers | 38.01 ± 0.06, 36.71 ± 0.18 | 28.25 ± 1.87 | 23.34 ± 0.29 |
| 4 layers | 75.11 ± 0.56, 71.78 ± 0.43 | 25.37 ± 3.47 | 13.83 ± 0.26 |
| 6 layers | 112.01 ± 0.42, 107.61 ± 0.13 | 25.33 ± 0.75 | 13.43 ± 0.21 |
| Conventional specimen | 50.11 ± 0.05, 49 ± 0.95 | 51.92 ± 1.85 | 50.82 ± 0.62 |

Fig. 10 shows the compressive strength test results of the printed specimens without glass fibre. The figure illustrates that printed structures possess lower mechanical strength compared to conventional specimens. This is particularly emphasized by the specimen with 6 layers. The compressive strength tests for each number of layers can be seen in Table 5, where the 2 layer specimen exhibited the highest result ($23.34 \pm 0.29$ MPa). The resulting compressive strength of the conventional mould is relatively high for mortar specimens ($50.82 \pm 0.62$ MPa). However, each specimen that incorporated glass fibre has a higher strength than its respective glass fibre-absent equivalent. This demonstrates that the glass fibre enhances the mechanical strength of the printed specimens rather than improving the strain property of the materials.

The inclusion of glass fibre in the printed specimens increased the strength twofold, compared to specimens without glass fibre. Comparing the 6 layers printed specimens in Fig. (10), the presence of 1% glass fibre increased the mechanical strength by 46.98%.

Overall, it was observed that the specimens containing the glass fibre demonstrated improved performance compared to specimens without glass fibre. In particular, once the strength of the specimens had reached yield, the mechanical strength of specimens possessing glass fibre had better performance in the strain hardening region. The cast specimens are shown to possess improved compressive strength characteristics, due to the process of vibrating the specimens to reduce its porosity. This improvement is attributed to the interactions between particles in the specimen, where close intermolecular interaction is induced due to the restrictive property of a mould [51].

Flexural moment of the printed member is high enough to be considered in structural calculations. Hence, the empirical flexural strengths of mortar were calculated for the 28 days of printed specimens, ~~equation~~Eq. (12). The maximum moment at the cracking stage ( $M_{cr}$ ) can be found as shown in ~~equation~~Eq. (13):

$$f't = 0.6\sqrt{f'c} \quad \textbf{(12)}$$

where $f't$ , is the modulus of rupture for mortar in MPa and $f'c$ is characteristic compressive strength in MPa, according to the Australian standard [51].

The cracking moment can be found for ( $M_{cr}$ ), utilising the following ~~equation~~Eq. (13):

$$M_{cr} = \frac{f't\, I}{y_t} \quad \textbf{(13)}$$

where $M_{cr}$ is a maximum moment in N mm, while $I$ is the second moment of area (moment of inertia) $mm^4$ and $b$ is width times to a depth of specimen's cross-section ( (space) $I$ ) divided by 12. The $y_t$ is the depth of the specimen to the neutral axis which is depth ($h$) divided by 2.

By using ~~equation~~Eq. (13), the cracking moments are determined and listed in Table 6 for the glass fibre-reinforced printed and conventional casted specimens. In addition, Table 7 represents a list of specimens made of plain mortar.

**Table 6** Results of the craking moment for the glass fibre reinforced printed specimens and conventional specimens.

alt-text: Table 6

| Specimen description | Width (mm) | Depth (mm) | $I$ ($mm^4$) | $f'c$ (average) ($N/mm^2$) | $f't$ ($N/mm^2$) | $M_{cr} \times 10^3$ |
|---|---|---|---|---|---|---|
| 1 | 20 | 20 | 13333.33 | 31.09 | 3.34550445 | 4.46 |
| 2 | 40 | 40 | 213333.3 | 28.25 | 3.18904374 | 34.01 |
| 4 | 80 | 80 | 3413333 | 25.37 | 3.02211846 | 257.88 |
| 6 | 120 | 120 | 17280000 | 25.33 | 3.01973509 | 869.68 |
| Casted | 40 | 40 | 213333.3 | 51.92 | 4.32333205 | 46.11 |

**Table 7** Results of the cracking moment for the non-reinforced printed specimens and conventional specimens.

alt-text: Table 7

| Specimen description | Width (mm) | Depth (mm) | $I$ ($mm^4$) | $f'c$ (average) ($N/mm^2$) | $f't$ ($N/mm^2$) | $M_{cr} \times 10^3$ |
|---|---|---|---|---|---|---|
| 1 | 20 | 20 | 13333.33 | 14.91 | 2.31680815 | 3.09 |
| 2 | 40 | 40 | 213333.3 | 23.34 | 2.89868936 | 30.91 |
| 4 | 80 | 80 | 3413333 | 13.83 | 2.23132248 | 190.41 |
| 6 | 120 | 120 | 17280000 | 13.43 | 2.19881786 | 633.26 |
| Casted | 40 | 40 | 213333.3 | 50.82 | 4.27728886 | 45.62 |

The results for the cracking moment of the three-point load are shown in the tables: Table (6) for the glass fibre reinforced, and Table (7) for non-reinforced printed specimens. The cracking moment strength ( $M_{cr}$ ) represents the highest moment before the failure of specimens. The effectiveness of fibre reinforcement is evident when comparing the results in Tables 6 and 7. The cracking moment varied from the 1~~st layer to the 6th~~st layer to the 6th layer at the fibre reinforced printed sections $4.46 \times 10^3$ to $869.68 \times 10^3$ N mm. These results changes for non-reinforced fibre $3.09 \times 10^3$ to $633.26 \times 10^3$ N mm. Hence, using glass fibre-reinforcement increases the moment capacity by 37.29 %

compared to non-reinforced printed specimens. In other words, the glass fibre reinforcement improves the moment capacity of the printed specimens. The glass fibre is mainly embedded in the parallel direction to printed specimens while printing. This further increases the bending strength and improves the bending stiffness.

The outcomes for the flexural strength tests of specimens containing 1 % glass fibre after curing for 28 days in tap water are presented in Fig. 11. The results show that the printed specimens with 2 layers have an approximate value of (8.69 ± 0.82 MPa), where the conventional mould had a result of (8.76 ± 0.92 MPa). Table 8 presents the flexural strength of the printed specimens. The flexural strength of the printed specimens with 1 layer, (9.03 ± 1.50 MPa) is greater than that of the specimen produced in the conventional mould. However, the calculated results for specimens with 4 and 6 layers were lower, (6.31 ± 0.60 Mpa) and (6.43 ± 0.52 Mpa), respectively. It is hypothesised that this is due to the increased number of voids in the multi-layer specimens.

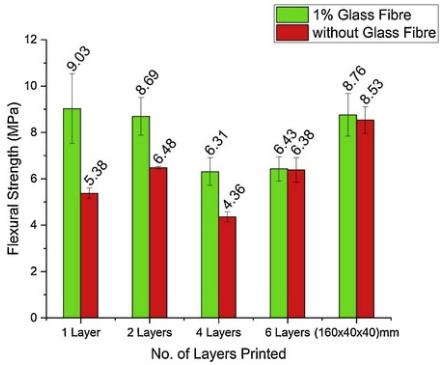


**Fig. 11** Flexural strength results (MPa) of printed cubic specimens with 1 % glass fibre, cured for 28 days.

alt-text: Fig. 11

**Table 8** Results of the flexural strength for the printed specimens and conventional specimens.

alt-text: Table 8

| Specimen description | Actual dimensions under three-point bending machine (mm) | Flexural strength (MPa) with 1 % glass fibre | Flexural strength (MPa) without glass fibre |
|---|---|---|---|
| 1 layer | 119.31 ± 0.14 × 19.18 ± 0.34 × 18.56 ± 0.61 | 9.03 ± 1.50 | 5.38 ± 0.22 |
| 2 layers | 159.95 ± 0.31 × 38 ± 0.06 × 36.71 ± 0.18 | 8.69 ± 0.82 | 6.48 ± 0.05 |
| 4 layers | 223.16 ± 0.23 × 75.11 ± 0.56 × 71.78 ± 0.43 | 6.31 ± 0.60 | 4.36 ± 0.21 |
| 6 layers | 259.05 ± 0.11 × 112.01 ± 0.42 × 107.61 ± 0.13 | 6.43 ± 0.52 | 6.38 ± 0.54 |
| Conventional specimen | 160.18 ± 0.08 × 40.11 ± 0.05 × 39.87 ± 0.95 | 8.76 ± 0.92 | 8.53 ± 0.58 |

The aforementioned outcomes support the work of Hambach and Volkmer [49] performed on cement paste printed specimens with 1 % (by volume) carbon fibre. Their results highlighted a 300 % increase in flexural strength (approximately 30 MPa) in printed specimens possessing 1 % carbon fibre. However, the results demonstrate that the mechanical strength of the second layer could be improved given the higher standard deviation in specimens incorporating glass fibre in the mortar mix.

Fig. 11 shows the flexural strength results of the printed specimens and conventional specimens without glass fibre. The graph indicates a fluctuation in the flexural strength of the printed specimen with 2 layers, however, it decreases at 4 layers. At 6 layers the flexural strength is (6.38 ± 0.54 MPa). However, these values are below those of the conventionally casted mould (8.53 ± 0.58 MPa). These results are also attributed to the increased number of voids as the printed layer count increases.

## 4.2 Presence of ~~Voids and C~~voids and cracks

Fig. 12 demonstrates the existence of voids created between each printed layer. These voids are observed when laying a successive layer on the existing layers. Consequently, the efficacy of the glass fibre is reduced after each

successive layer due to the gaps that are created by this process. Fig. 12 demonstrates that the voids are more apparent after the 4$^{th}$ layer of the print. These voids are the major contributing factor in reducing the flexural strength of the printed mortar, where the average area of the voids is approximately $25 \pm 5$ mm$^2$. This measurement was obtained using ImageJ software, where the freehand selection tool enabled the area to be calculated.

**Fig. 12** Cross-section of specimen demonstrating voids (colored red) amongst the printed mortar layers with an average area of 25 mm$^2$. (For interpretation of the references to colour in this figure legend, the reader is referred to the web version of this article.).

alt-text: Fig. 12

Based on the aforementioned observations, the performance of the 3DP specimens is known to be significantly affected by the design of the specimen. Since concrete 3DP structures are not limited to mould based designs, this technique can be used to construct solid specimens, hollow partitions, or even walls. Fig. 12 demonstrates that the existing voids in the structure have been unintentionally introduced due to the shape and size of the nozzle used, and the 3DP slicing parameters (e.g. fill density and thickness). The size and shape of these voids can be minimised by the speed of the end-effector, the selection of nozzle shape and size, and height of the nozzle from the desired printing surface.

The additional superplasticizer (see Table (2)) in the glass fibre mixtures was incorporated to aid the flow of material through the delivery system, however, the high ratio of superplasticizer also accelerated the concrete setting time causing cracks to form in the specimens [52]. Using a larger amount of superplasticizer can significantly affect the early age physical properties of the printed objects. For this study, the ratio of superplasticizer in both mixtures, with and without glass fibre, differs by 5 mL. The additional superplasticizer improves the rheological fluctuation of the two mixtures [53], however, further study is required to determine the degree to which the superplasticizer ratio affects the mechanical behaviour of early age specimens.

## 4.3 Print ~~Quality Relative to Robotic M~~quality relative to robotic motion

From the examined specimens, it was observed that the properties of the structure were also influenced by the end-effector motion. In this section, the result of the end-effector velocity in relation to the slurry discharge and width of the printed specimen is discussed.

Fig. 13 illustrates the relationship between the velocity of the end-effector (mm/s), the amount of slurry discharged (g), and the printed line width (mm). The end-effector velocity used during the experiments varied from 11.99 mm/s to 98.88 mm/s, at intervals of approximately 12 mm/s.

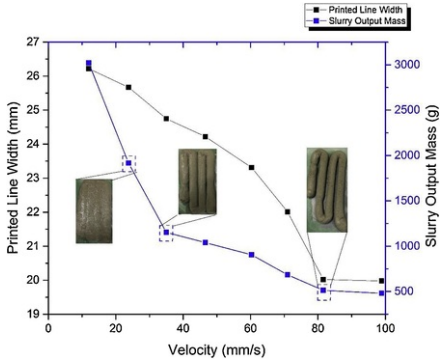


**Fig. 13** Velocity (mm/s) in relation to printed line width (mm) and slurry output mass (g).

alt-text: Fig. 13

To ensure the mortar mixture is deposited uniformly, the extruder is required to travel at a constant velocity. In addition, the presence of humans in the robot's workspace requires the constant end-effector velocity performed by the robotic arm to fall within the 'safe zone' defined by [21]. Therefore, a defined safe maximum velocity for the robotic arm is imperative to facilitate a safe work environment.

Fig. 14 shows the corresponding printed specimens for the variously defined velocities. It was observed that end-effector velocities of 34.99 mm/s, 46.56 mm/s and 60.32 mm/s yielded the best specimens when considering the shapeability and continuity of the printed line.


**Fig. 14** Photographs showing the resulting output shape of mortar at various end-effector velocities.

alt-text: Fig. 14

The corresponding printed line width of each end-effector velocity can be seen in Table 9. In this study, the prismatic and cubic specimens were printed using end-effector velocities of up to 34.99 mm/s.

**Table 9** Width of the printed line versus velocity.

alt-text: Table 9

| Velocity (mm/s) | Width of the printed line (mm) |
|---|---|
| 11.96 | 26.22 |
| 23.78 | 25.67 |
| 34.99 | 24.75 |
| 46.56 | 24.22 |
| 60.32 | 23.31 |
| 70.97 | 22.01 |
| 81.56 | 20.02 |
| 98.88 | 19.98 |

Consequently, it was hypothesised that the optimum end-effector velocity is 81.56 mm/s, for a printed line width corresponding to a nozzle diameter of 20 mm, see Fig. 13. Fig. 14 emphasizes the effect of the end-effector velocity on the structural integrity of the specimen.

It was observed that an end-effector velocity of 60.32 mm/s caused a slight shrinkage and discontinuous among particles of the specimen, resulting in cracks on the surface of the fresh mortar specimen. Therefore, ideal end-effector velocities for the mortar mix designed in this study were in the range of 34.99 mm/s to 46.56 mm/s. Furthermore, Fig. 14 demonstrates that end-effector velocities below 34.99 mm/s and greater than 45.56 mm/s result in observable cracks in the specimens, discontinuous print segments and undesired shape structures. These results are consistent with studies by Thrane, Pade and Nielsen [54] and Buswell, Leal de Silva, Jones and Dirrenberger [1].

Since the process for 3DP involves the layer by layer deposition of materials, single layer specimens were shown in Fig. 14 to highlight the visually observable differences between the varying velocities.

Fig. 15 shows the power regression relationship for velocity euquation (14):

$$Y = 28996X^{-0.884} \#$$

**(14)** **(please remove the symbol "#" after the equation.)**

where $Y$ describes the slurry discharge (g) from the nozzle, and $X$ describes the velocity (mm/s) of the end-effector of the robot (i.e. the tip of the nozzle relative to the surface). The equation fit the data with an R-squared value equal to 0.98, where R-squared is a measure describing how closely the data fit the regression line and a value closer to 1 is said to be a precise fit. The grey rectangle in Fig. 15 was found to be the ideal printable region, since the slurry discharge and the end-effector velocity can be consistently maintained, and the shapeability of the printed specimen is desirable.

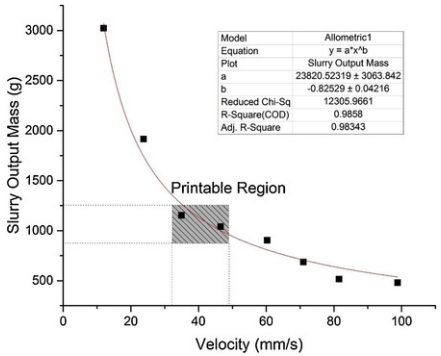


**Fig. 15** Power regression relationship between velocity and slurry output mass of the printed mortar line without glass fibre.

alt-text: Fig. 15

The effect of the robot end-effector velocity, resulting deposition of the printed mortar line width, and slurry discharge, as well as the effect of glass fibre on the printed mortar specimens have been demonstrated in this paper.

More investigations are required to accurately disclose the bounds of the printable region window (Fig. 15) in the presence of glass fibre. Previous studies have shown that the presence of glass fibre is capable of affecting the final result of the printed line and can lead to reducing space between particles [31]. Thus, reducing the plastic shrinkage on the surface of the printed line and using glass fibre, is predicted to increase the printable end-effector velocity region up to 60.32 mm/s. Similarly, the flow rate of the pump can affect the printed specimen. For this study, a constant flow rate was selected, however, further study is required to quantify the interaction between the pump flow rate and end-effector velocity.

Vision-based sensing has been incorporated into systems for 3D printing with robotic arms [55]. Such a system could be adapted for mortar and concrete printing to make on-the-fly assessments using image analysis techniques, and correct robot motions (and pump settings) to ensure accurate deposition and slurry flow discharge. Further investigation is required to measure the observed shrinkage of printed mortar and concrete with conventional cast methods [56].

# 5 Conclusions

3D printing of mortar still faces various challenges. In this study, the mortar mix of ordinary Portland cement, fine sand and glass fibre reinforcement were used to produce a robust structural mortar mix for construction applications. Additionally, ideal mix designs for cement mortar in the presence and absence of glass fibre as reinforcement have been described.

- The results demonstrate the orientation of glass fibres in the printed specimens, and the findings support observations in previous studies. It has been found that the addition of 1 % (by weight of cementitious material) glass fibre resulted in an increase of compressive and flexural strength by approximately 108~~% and 68~~ % and 68 %, respectively when compared to specimens without glass fibre reinforcement.
- A laser scanning microscope and ImageJ were used to show the number and alignment of fibre filaments embedded in the printed line. It was observed that approximately 80 % of the fibre orientation aligned with the nozzle's travel orientation.
- A safety-focused industrial robot end-effector orientation and velocity (i.e. nozzle travel) control approach is detailed, which demonstrates the viability of fabricating novel, mortar-based structures. The robot can thus adhere to safety constraints and avoid singularities while accurately tracking an adaptable trajectory with constant mortar deposition speeds.
- ImageJ was adjusted by selecting a coloured threshold to indicate the gap and void between the top and bottom layers. The results show a gap with an average width of 6000 µm and depth of 1700 µm between the top and bottom layers. Also observed were small pores and voids on the surface of the specimen resulting from chemical additives. The average diameter of the voids on the printed specimen was $350.24 \pm 101$ µm.
- This study also defined the nonlinear curve-fit of the allometric relationship between the end-effector velocity of the robot and the slurry output mass. In addition, the results highlight the effect of the robot end-effector velocity in relation to the shapeability and surface texture of the printed structures.

The use of robotic arms in 3DP with fibre reinforcement offers an alternative to conventional methods for constructing structures, as well as providing a means to create structures possessing internal or complicated geometries. Further development of printing and testing evaluations is required to decrease the voids and porosity in the specimens. Future studies to investigate the effect of the pumping process, and printhead orientation on the mechanical properties of the printed specimens is essential.

# Author ~~Contribution S~~contribution statement

Pshtiwan Shakor and Sheila Sutjipto; writing the draft of the manuscript and collecting the data. Shami Nejadi; supervising civil engineering work. Gavin Paul; supervising mechatronic engineering works. Review and Editing; the whole paper has been revised by Shami and Gavin. Final Revision and Correction; has been done by Nadarajah Gowripalan. Terminology and Format of the paper; checked also by Nadarajah Gowripalan.

# Declaration of Competing Interest

We wish to confirm that there are no known conflicts of interest associated with this publication and there has been no significant financial support for this work that could have influenced its outcome.

# Acknowledgement

The authors would like to thank UTS-TechLab (Civil Engineering laboratory and the Centre for Autonomous Systems laboratory) for their support, and the Sika Australia company for providing the admixtures.

# Appendix A. Supplementary data

Supplementary material related to this article can be found, in the online version, at doi:https://doi.org/10.1016/j.addma.2020.101069.(Please **delete these videos**, which has been added as an Appendix A. Supplementary data. These videos just for the reviewer.)

# References


**[1]** R.A. Buswell, W.R. Leal de Silva, S.Z. Jones and J. Dirrenberger, 3D printing using concrete extrusion: Aa roadmap for research, *Cement and Concrete Research. Concr. Res.* **112**, 2018, 37–49, https://doi.org/10.1016/j.cemconres.2018.05.006.

**[2]** R.A. Buswell, R. Soar, A.G. Gibb and T. Thorpe, The potential of freeform construction pPotential of Freeform Construction Processes, https://repository.lboro.ac.uk/articles/The_potential_of_freeform_construction_processes/9434630, 2005.

**[3]** L. Edwards, C. Holt, L. Keyte and R. Lloyd, Construction 3D Printing, Concrete 2013, 2013, Gold Coast; Australia.

**[4]** I. Gibson, D. Rosen and B. Stucker, Additive Manufacturing Technologies: 3D Printing, Rapid Prototyping, and Direct Digital Manufacturing, 2015, Springer-Verlag New York; New York, https://doi.org/10.1007/978-1-4939-2113-3.

**[5]** Y.W.D. Tay, B. Panda, S.C. Paul, N.A. Noor Mohamed, M.J. Tan and K.F. Leong, 3D printing trends in building and construction industry: a review, *Virtual and Physical PrototypingPhys. Prototyp.* **12** (3), 2017, 261–276, https://doi.org/10.1080/17452759.2017.1326724.

**[6]** T.T. Le, S.A. Austin, S. Lim, R.A. Buswell, R. Law, A.G. Gibb and T. Thorpe, Hardened properties of high-performance printing concrete, *Cement and Concrete Research. Concr. Res.* **42** (3), 2012, 558–566, https://doi.org/10.1016/j.cemconres.2011.12.003.

**[7]** B. Khoshnevis, Automated construction by contour crafting—related robotics and information technologies, *Automation in construction. Constr.* **13** (1), 2004, 5–19, https://doi.org/10.1016/j.autcon.2003.08.012.

**[8]** C. Gosselin, R. Duballet, P. Roux, N. Gaudillière, J. Dirrenberger and P. Morel, Large-scale 3D printing of ultra-high performance concrete – a new processing route for architects and builders, *Materials & Design. Des.* **100**, 2016, 102–109, https://doi.org/10.1016/j.matdes.2016.03.097.

**[9]** P. Wu, J. Wang and X. Wang, A critical review of the use of 3-D printing in the construction industry, *Automation in Construction. Constr.* **68**, 2016, 21–31, https://doi.org/10.1016/j.autcon.2016.04.005.

**[10]** S.C. Paul, G.P. van Zijl, M.J. Tan and I. Gibson, A review of 3D concrete printing systems and materials properties: Ccurrent status and future research prospects, *Rapid Prototyping Journal. J.* **24** (4), 2018, 784–798, https://doi.org/10.1108/RPJ-09-2016-0154.

**[11]** S. Lim, R.A. Buswell, P.J. Valentine, D. Piker, S.A. Austin and X. De Kestelier, Modelling curved-layered printing paths for fabricating large-scale construction components, *Additive Manufacturing 12, Part B* 2016, 216–230, https://doi.org/10.1016/j.addma.2016.06.004.

**[12]** V. Mechtcherine and V.N. Nerella, 3D Printing with concrete: Sstate-of-the art, trends, challenges, *Bautechnik* **95** (4), 2018, 275–287.

**[13]** F.P. Bos, Z.Y. Ahmed, R.J.M. Wolfs and T.A.M. Salet, 3D Printing Concrete wWith Reinforcement, 2018, Springer International Publishing; Cham, 2484–2493, https://doi.org/10.1007/978-3-319-59471-2_283.

**[14]** A. Paolini, S. Kollmannsberger and E. Rank, Additive manufacturing in construction: Aa review on processes, applications, and digital planning methods, *Additive Manufacturing. Manuf.* **30**, 2019, , 100894https://doi.org/10.1016/j.addma.2019.100894.

**[15]** Y. Nakamura and H. Hanafusa, Inverse Kinematic Solutions With Singularity Robustness for Robot Manipulator ControlJournal of dynamic systems, measurement, and ekinematic solutions with singularity robustness for robot manipulator control, *J. Dyn. Syst. Meas. Control* **108** (3), 1986, 163–171, https://doi.org/10.1115/1.3143764.

**[16]** M.G. Carmichael, D. Liu and K.J. Waldron, A framework for singularity-robust manipulator control during physical human-robot interaction, *The International Journal of Robotics ResearchInt. J. Rob. Res.* **36** (5-7), 2017, 861–876, https://doi.org/10.1177/0278364917698748.

**[17]** P. Shakor, J. Renneberg, S. Nejadi and G. Paul, Optimisation of different concrete mix designs for 3D Pprinting by utilising 6DOF industrial robot, In: *ISARC 2017-Proceedings of the 34th International Symposium on Automation and Robotics in Construction,* 2017https://doi.org/10.22260/ISARC2017/0036.

**[18]** A.M. Zanchettin, N.M. Ceriani, P. Rocco, H. Ding and B. Matthias, Safety in human-robot collaborative manufacturing environments: Mmetrics and control, *IEEE Transactions on Automation Science and Engineering. Autom. Sci. Eng.* **13** (2), 2015, 882–893, https://doi.org/10.1109/TASE.2015.2412256.

**[19]** I.-, Robots and robotic devices Safety requirements for industrial rRobotic Devices — Safety Requirements for Industrial Robots Part 2, Robot systems and integration Geneva; Switzerland, https://www.iso.org/standard/41571.html, 2011.

**[20]** I., 10218-1:2011, Robots and robotic devices Safety requirements for industrial rRobotic Devices — Safety Requirements for Industrial Robots — Part 1, Robots; Geneva, Switzerland, https://www.iso.org/standard/51330.html, 2011.

**[21]** Y. Beauchamp, T.J. Stobbe, K. Ghosh and D. Imbeau, Determination of a safe slow robot motion speed based on the effect of environmental factors, *Human rl. Factors* **33** (4), 1991, 419–427, https://doi.org/10.1177/001872089103300404.

**[22]** G.W. Clark, M.V. Doran and T.R. Andel, Cybersecurity issues in robotics, In: *IEEE Conference on Cognitive and Computational Aspects of Situation Management (CogSIMA),* IEEE2017, 1–5, https://doi.org/10.1109/COGSIMA.2017.7929597.

**[23]** A. Faruque, M. Abdullah, S.R. Chhetri, A. Canedo and J. Wan, Acoustic side-channel attacks on additive manufacturing systems, In: *Proceedings of the 7th International Conference on Cyber-Physical Systems,* IEEE Press2016, 19 https://dl.acm.org/citation.cfm?id=2984483.

**[24]** J. Teizer, A. Blickle, T. King, O. Leitzbach and D. Guenther, Large Scale 3D Printing of Complex Geometric Shapes in Cscale 3D printing of complex geometric shapes in construction, In: *ISARC. Proceedings of the International Symposium on Automation and Robotics in Construction, Vilnius Gediminas Technical University, Department of Construction Economics & Property,* 2016, 1, https://doi.org/10.22260/ISARC2016/0114.

**[25]** B. Utela, D. Storti, R. Anderson and M. Ganter, A review of process development steps for new material systems in three dimensional printing (3DP), *Journal of Manufacturing Processes. Manuf. Process.* **10** (2), 2008, 96–104, https://doi.org/10.1016/j.jmapro.2009.03.002.

**[26]** S. Lim, R.A. Buswell, T.T. Le, R. Wackrow, S.A. Austin, A.G.F. Gibb and T. Thorpe, Development of a viable concrete printing pViable Concrete Printing Process, https://repository.lboro.ac.uk/articles/Development_of_a_viable_concrete_printing_process/9437288, 2011.

**[27]** J. Xu, L. Ding, L. Cai, L. Zhang, H. Luo and W. Qin, Volume-forming 3D concrete printing using a variable-size square nozzle, *Automation in Construction. Constr.* **104**, 2019, 95–106, https://doi.org/10.1016/j.autcon.2019.03.008.

**[28]** Y.W.D. Tay, M.Y. Li and M.J. Tan, Effect of printing parameters in 3D concrete printing: Pprinting region and support structures, *journal of Materials Processing Technology. Mater. Process. Technol.* **271**, 2019, 261–270, https://doi.org/10.1016/j.jmatprotec.2019.04.007.

**[29]** F. Bos, R. Wolfs, Z. Ahmed and T. Salet, Additive manufacturing of concrete in construction: potentials and challenges of 3D concrete printing, *Virtual and Physical PrototypingPhys. Prototyp.* **11** (3), 2016, 209–225, https://doi.org/10.1080/17452759.2016.1209867.

**[30]** T.T. Le, S.A. Austin, S. Lim, R.A. Buswell, A.G.F. Gibb and T. Thorpe, Mix design and fresh properties for high-performance printing concrete, *Materials and Structures. Struct.* **45** (8), 2012, 1221–1232, https://doi.org/10.1617/s11527-012-9828-z.

**[31]** P. Shakor, S. Nejadi and G. Paul, A Study into the Effect of Different Nozzles Shapes and Fibre-Reinforcement in 3D Printed Mstudy into the effect of different nozzles shapes and fibre-reinforcement in 3D printed mortar, *Materials* **12** (10), 2019, 1708, https://doi.org/10.3390/ma12101708.

**[32]** Z. Malaeb, H. Hachem, A. Tourbah, T. Maalouf, N. El Zarwi and F. Hamzeh, 3d Concrete Printing: Machine And Mix DesignInternational Journal of Civil Engineeringconcrete printing: machine and mix design, *Int. J. Civ. Eng.* (6), 2015 https://pdfs.semanticscholar.org/334f/311902b286bd225b11a2cdbd49e387cd2405.pdf.

**[33]** R.J. Boring, Rotary lobe pumps versus progressive cavity pLobe Pumps Versus Progressive Cavity Pumps, https://www.flowcontrolnetwork.com/pumps-motors-drives/article/15563439/rotary-lobe-pumps-versus-progressive-cavity-pumps, 2016.

**[34]** C.E. Bakis, L.C. Bank, V. Brown, E. Cosenza, J. Davalos, J. Lesko, A. Machida, S. Rizkalla and T. Triantafillou, Fiber-reinforced polymer composites for construction—State-of-the-art review, *Journal of composites for construction*. *Compos. Constr.* **6** (2), 2002, 73–87, https://doi.org/10.1061/(ASCE)1090-0268(2002)6:2(73).

**[35]** F.P. Bos, E. Bosco and T.A.M. Salet, Ductility of 3D printed concrete reinforced with short straight steel fibers, *Virtual and Physical Prototyping Phys. Prototyp.* **14** (2), 2019, 160–174, https://doi.org/10.1080/17452759.2018.1548069.

**[36]** B. Panda, S.C. Paul and M.J. Tan, Anisotropic mechanical performance of 3D printed fiber reinforced sustainable construction material, *Materials Letters. Lett.* **209**, 2017, 146–149, https://doi.org/10.1016/j.matlet.2017.07.123.

**[37]** S.C. Paul, G.P.A.G. van Zijl, M.J. Tan and I. Gibson, A review of 3D concrete printing systems and materials properties: current status and future research prospects, *Rapid Prototyping Journal. J.* **24** (4), 2018, 784–798, https://doi.org/10.1108/RPJ-09-2016-0154.

**[38]** Y.W. Tay, B. Panda, S.C. Paul, M.J. Tan, S.Z. Qian, K.F. Leong and C.K. Chua, Processing and properties of construction materials for 3D printing, Materials Science Forum, *Trans Tech Publ. Tech. Publ.* 2016, 177–181, https://doi.org/10.4028/www.scientific.net/MSF.861.177.

**[39]** JushiUSA, Chopped Strands 552B for BMC. http://jushiusa.com/.

**[40]** TheAmericanCeramicSociety, New E6 enhanced glass fiber iEnhanced Glass Fiber Introduced, https://ceramics.org/ceramic-tech-today/new-e6-enhanced-glass-fiber-introduced-2, 2009.

**[41]** AS1012.9, Methods of testing cTesting Concrete - Compressive strength tests - Concrete, mortar and grout sStrength Tests - Concrete, Mortar and Grout Specimens, 2014, https://infostore.saiglobal.com/en-us/Standards/AS-1012-9-2014-111734_SAIG_AS_AS_233709/, 2014.

**[42]** ASTMC293/C293M, 293 Standard Test Method for Flexural Strength of Concrete (Using Simple Beam With Center-Point Loading), ASTM; Standard, http://www.astm.org/cgi-bin/resolver.cgi?C293C293M, 2002.

**[43]** T. Yoshikawa, Manipulability of robotic mechanisms, *The international journal of Robotics Research Int. J. Rob. Res.* **4** (2), 1985, 3–9, https://doi.org/10.1177/027836498500400201.

**[44]** Pumps, In: E.W. McAllister, (Ed), *Pipeline Rules of Thumb Handbook (Eighth Edition),* 2014, Gulf Professional Publishing; Boston, 471–540 https://www.bookdepository.com/Pipeline-Rules-Thumb-Handbook-E-W-McAllister/9780123876935.

**[45]** NEMOPumpBO/BS, NEMO® BO/BS Pump with Hopper in Block Construction and Flanged Drive. https://pumps.netzsch.com/en/products-accessories/nemo-progressing-cavity-pumps/nemo-pump-bobs/.

**[46]** A. El-Haroun, Environment Cconservation through the Use of Wind EnergyJournal of Fundamentals of Renewable Energy and Applicationsuse of wind energy, *J. Fundam. Renew. Energy Appl.* **1**, 2011 http://journaldatabase.info/articles/environment_conservation_through_use.html.

**[47]** D.G. Soltan and V.C. Li, A self-reinforced cementitious composite for building-scale 3D printing, *Cement and Concrete Composites. Concr. Compos.* **90**, 2018, 1–13, https://doi.org/10.1016/j.cemconcomp.2018.03.017.

**[48]** B.G. Compton and J.A. Lewis, 3D-printing of lightweight cellular composites, *Advanced materials. Mater.* **26** (34), 2014, 5930–5935, https://doi.org/10.1002/adma.201401804.

**[49]** M. Hambach and D. Volkmer, Properties of 3D-printed fiber-reinforced Portland cement paste, *Cement and Concrete Composites. Concr. Compos.* **79**, 2017, 62–70, https://doi.org/10.1016/B978-0-12-815481-6.00005-1.

**[50]** K. Choo, B. Friedrich, T. Daugherty, A. Schmidt, C. Patterson, M.A. Abraham, B. Conner, K. Rogers, P. Cortes and E. MacDonald, Heat retention modeling of large area additive manufacturing, *Additive Manufacturing. Manuf.* **28**, 2019, 325–332, https://doi.org/10.1016/j.addma.2019.04.014.

**[51]** F. Wittmann, Interaction of hardened cement paste and water, *Journal of the American ceramic society. Am. Ceram. Soc.* **56** (8), 1973, 409–415, https://doi.org/10.1111/j.1151-2916.1973.tb12711.x.

**[52]** O. Esping and I. Löfgren, Investigation of early age deformation in self-compacting concrete, In: *the Knud Højgaard cConference on Advanced Cement-Based Materials-Research and Teaching,* 2005https://doi.org/10.1617/2351580052.027.

**[53]** J. Katzer and T. Szatkiewicz, Properties of concrete elements with 3-D printed formworks which substitute steel reinforcement, *Construction and Building Materials. Build. Mater.* **210**, 2019, 157–161,

https://doi.org/10.1016/j.conbuildmat.2019.03.204.

**[54]** L.N. Thrane, C. Pade and C.V. Nielsen, Determination of rheology of self-consolidating concrete using the 4C-Rheometer and how to make use of the results, *Journal of ASTM International. ASTM Int.* **7** (1), 2009, 1–10, https://doi.org/10.1520/JAI102003.

**[55]** S. Sutjipto, D. Tish, G. Paul, T. Vidal-Calleja and T. Schork, Towards Visual Feedback Loops for Robot Controlled Additive Mvisual feedback loops for robot-controlled additive manufacturing, In: J. Willmann, P. Block, M. Hutter, K. Byrne and T. Schork, (Eds.), *Robotic Fabrication in Architecture, Art and Design 2018,* 2019, Springer International Publishing; Cham, 85–97 https://www.springerprofessional.de/en/towards-visual-feedback-loops-for-robot-controlled-additive-manu/16073162.

**[56]** A.C.L. Wong, P.A. Childs, W. Terry, N. Gowripalan and G.-D. Peng, Experimental Investigation of Drying Shrinkage and Creep of Concrete Using Fibre Optic SensorsAdvances in Structural Engineeringinvestigation of drying shrinkage and creep of concrete using fibre-optic sensors, *Adv. Struct. Eng.* **10** (3), 2007, 219–228, https://doi.org/10.1260/136943307781422262. [57] P. Shakor, S. Nejadi, G. Paul, S. Malek, Review of Emerging Additive Manufacturing Technologies in 3D Printing of Cementitious Materials in the Construction Industry, Frontiers in Built Environment 4(85) (2019) https://doi.org/10.3389/fbuil.2018.00085. [58] P. Shakor, S. Nejadi, G. Paul, J. Sanjayan, A. Nazari, Mechanical Properties of Cement-Based Materials and Effect of Elevated Temperature on Three-Dimensional (3-D) Printed Mortar Specimens in Inkjet 3-D Printing, ACI Materials Journal 116(2) (2019) 55-67 https://doi.org/10.14359/51714452.

# Appendix A. Supplementary data

The following are Supplementary data to this article: (Please remove all multimedia components are not necessary.)

Multimedia Component 1

Multimedia Component 2 

Multimedia Component 3 

**Graphical abstract**

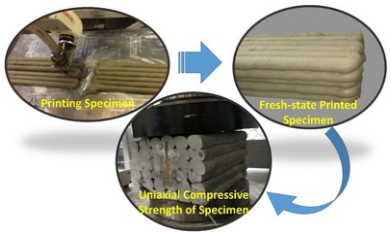


**Highlights**

- Effect of deposition velocity on the width, continuity and mechanical properties of printed mortar.
- The pumping flow rate influences the printed mortar specimens.
- Mechanical strength of printed specimens with various printed layers in the presence/absence of glass fibre, compared with moulded mortar.
- Versatile nature of an industrial robot when fabricating novel forms through an adaptable end-effector orientation and velocity control approach.

## Queries and Answers

**Query:** The resolution of Figure 1 is too low to be used. Please provide better quality of Figure 1.
**Answer:** Sure, it has been replaced to a better resolution Figure1.
**Attachments:** Figure 1.jpg

**Query:** Please check the correctness of Fig. 1 and correct if necessary.
**Answer:** That is fine.

**Query:** Figs. 8 and 12 will appear in black and white in print and in color on the web. Based on this, the respective figure captions have been updated. Please check, and correct if necessary.
**Answer: Fig. 8 Voids and gaps between layers can be distinguished from the printed surface using colour coding (for an interpretation of the references to colour in this figure's legend, the reader is referred to the web version of this article.)**

**Query:** Your article is registered as a regular item and is being processed for inclusion in a regular issue of the journal. If this is NOT correct and your article belongs to a Special Issue/Collection please contact e.maruthu@elsevier.com immediately prior to returning your corrections.
**Answer:** All good.

**Query:** The author names have been tagged as given names and surnames (surnames are highlighted in teal color). Please confirm if they have been identified correctly.
**Answer:** Yes

**Query:** Highlights must be provided as 3-5 bullet points, each bullet point having a maximum of 125 characters. Please rephrase the following highlights or provide new highlights.
**Answer: bullet point three:** Mechanical strength of multi-layered printed specimens in the presence/absence of glass fibre, compared with moulded mortar. **bullet point four:** An adaptable industrial robot end-effector orientation and velocity control approach for versatile novel form fabrication.
**Attachments:** highlights.docx

**Query:** Please check the hierarchy of the section headings.
**Answer:** Ok, all good.

**Query:** Have we correctly interpreted the following funding source(s) and country names you cited in your article: UTS-TechLab?
**Answer:** Sheila Sutjipto is supported by Australian Government Research Training Program Scholarships.